Stress-Induced Changes in Microstructure of a Low-Crystalline Polypropylene Investigated at Uniaxial Stretching

A. Boger,[1,2] C. Imhof,[1] B. Heise,[1] O. Marti,[1] C. Troll,[3] B. Rieger,[3] S. Hild[1,4]

[1]*Experimental Physics, University of Ulm, 89081 Ulm, Germany*
[2]*Synthes GmbH, Biomaterials, Eimattstrasse 3, 4436 Oberdorf, Switzerland*
[3]*Macromolecular Chemistry, Technical University Munich, 85747 Garching, Germany*
[4]*Max-Planck Institut für Eisenforschung, 40237 Düsseldorf, Germany*

Received 2 June 2008; accepted 5 September 2008
DOI 10.1002/app.29282
Published online 22 December 2008 in Wiley InterScience (www.interscience.wiley.com).

ABSTRACT: Novel asymmetric metallocene catalysts lead to low isotactic polypropylenes (iPP) with randomly distributed stereo irregularities. The polypropylenes are low crystalline and show elastic mechanical behavior due to physical crosslinking. The morphology of such iPP, which is responsible for the observed mechanical properties, is still sparsely resolved. In the present work a low isotactic, low crystalline metallocene iPP containing randomly distributed stereoerrors was investigated. The influence of the chain microstructure in the elastic properties was studied using two complementary investigation methods, X-ray diffraction and scanning force microscopy (SFM). For a better understanding of the unique mechanical properties, microscopic changes in morphology and strain-induced variation in chain orientation were monitored during uniaxial stretching using SFM and wide angle X-ray scattering measurements. For quantitative analysis and discussion the polymer chain orientations were calculated. The correlation between the orientation, the arrangements of the amorphous and crystalline phases observed by SFM, and the mechanical properties of the material at different elongation ratios allowed an interpretation of the macroscopic behavior on the microscopic scale. It was shown that the deformation behavior of low isotactic polypropylene with randomly distributed stereoerrors is in agreement with existing structural models, which proposed that small crystalline domains act as physical crosslinks for the amorphous matrix. © 2008 Wiley Periodicals, Inc. J Appl Polym Sci 112: 188–199, 2009

Key words: atomic force microscopy (AFM); WAXS; poly(propylene) (PP); mechanical properties; elastomers

INTRODUCTION

In the last decade, metallocene catalysts rapidly gained interest in academic research as well as in industrial development.[1] They provide the control over the chain microstructures of polyolefines in contrast to the conventional Ziegler-Natta catalysts.[2–11] When applied to propene polymerization,[12,13] depending on the symmetry of the catalyst and the polymerization conditions, a great variety of polypropylene polymers with different stereo regularities and molecular weight distributions can be polymerized resulting in samples not only with different crystallinities but also with different morphologies and physical properties.[7,8–10,14,15] Good examples of these variations are polypropylene with highly syndiotactic-, hemi-isotactic chains[7,8–10] or atactic-isotactic block structures.[11] Especially low crystalline polypropylenes (PP) have attracted an increasing amount of interest because these polymers exhibit elastomeric properties.[6,7,16–18] The elastic properties of these polypropylenes are assigned to a block structure of the chain where regular isotactic and irregular atactic sequences are present.[19–21] Studies performed on stereoblock isotactic-atactic polypropylenes[22–30] confirm the model that regular (isotactic) segments form small, stable crystals, which are randomly distributed in a soft matrix composed of the atactic chain segments.[5,22–26] The hard elements act as crosslinks and build up the network necessary for the elastic deformation. For amorphous thermoplastic elastomers, such as styrene butadiene copolymers, it is well known that not only the total number of hard segments but also their distribution within the chain determines the mechanical properties.[31]

Although a broad variety of low isotactic polypropylenes (iPP) have been synthesized,[3,8–11,27,32–40] the influence of the distribution of regular segments on their morphology and elastomeric behavior is not well understood. In this article, the strain-induced changes of a low isotactic polypropylene with

Correspondence to: A. Boger (boger.andreas@synthes.com).

statistically distributed stereo errors[8–10,15] were studied. Hence the isotactic blocks are short only small lamellar domains can be formed. These lamellae are able to provide a randomly distributed continuous network.[41] Properties, such as strength at elongation, are associated with rearrangement and deformation of the crystalline and amorphous domains. Therefore, the influence of the chain microstructure on the deformation process of elastomeric semicrystalline materials has to be investigated at the submicrometer level. Mechanical studies on semicrystalline polymers clearly show that properties such as tensile strength, elongation to break, and reversible deformation are associated with the rearrangement and deformation of the hard segment domains and amorphous domains. Based on many studies of highly oriented semicrystalline polymers, the microscopic process of tensile deformation was proposed to proceed within several regimes.[42–51] At first, intralamellar slipping of crystalline blocks occurs at small deformation when the strain is below the yield strain. At larger strain than the yield strain, a stress-induced crystalline block disaggregation-recrystallization process takes place. In contrast to the highly oriented semicrystalline polymers, for low-crystalline thermoplastic elastomers (TPE) a deformation process reminiscent of that observed in naturally occurring fibrous proteins such as silks[52] was proposed, where the breakup of crystallites and their orientation into fibrils were suggested to be the crucial processes during mechanical deformation.[3,28,53,54] Based on WAXS[3] and SFM[28] studies, three stages in the deformation were found.[3,28,53,54] In the unstrained state, flexible amorphous chains connect the randomly distributed crystalline domains. Under low deformation the amorphous regions are extended, and due to local stresses the crystalline domains break up. The rotation of domains and the selective breakup of hard domains at various orientations results in a structure containing small blocks aligned in the stretching direction at higher elongation. Thus, a fibrillar superstructure is formed where chains are oriented parallel to the stress direction, and the soft segment chains undergo stress-induced crystallization. Releasing the stress, the amorphous domains are preferentially retracted to reach the entropically favored disordered random coil conformation. Thus, the entropic effect is responsible for the elastic recovery.[53]

To learn more about the structural changes and crystal orientations of a low isotactic polypropylene containing statistically distributed stereoerrors, this study was performed using both WAXS and SFM experiments. Interpretations of the macroscopic mechanical behavior on the basis of chain orientations recorded from WAXS measurements on low crystalline, high molecular weight metallocene PPs give no final explanation of the mechanical behavior of those unique materials.[55] However, a number of publications showed that SFM has an excellent potential for studying polymers under macroscopic deformation.[28,53,56–59] One advantage of this method is that no thin film sectioning, staining, and sputtering is required as in the transmission electron microscopy. Thus, macroscopically thick samples can be studied on-line at different elongations. In this study, we investigated a low isotactic polypropylene film with SFM in both the nonstretched state and at different strains to correlate those results with WAXS observations. Strain-induced changes in the arrangements of the amorphous and crystalline phases were recorded in the SFM images and correlated to the orientation function of the existing crystals in the α- and γ-modification,[15] which were mainly received from a previous study.[55] The combination of the two methods allows the direct comparison to the novel findings received from the SFM investigations to obtain a better insight in the unique mechanical behavior of this material. The discussion of the orientation in terms of the main present net planes, arrangements of the phases, and stress strain measurements showed that the network, which is responsible for the elasticity, is mainly composed of strain-induced morphology changes combined to chain orientations.

EXPERIMENTAL SECTION

Materials

Sample preparation

A low isotactic polypropylene was prepared in toluene at 308 K using a C_1-symmetric *ansa*-zirconocene catalyst as described in Refs 8–10. Molecular weight and molecular weight distributions were determined by gel permeation chromatography (Alliance GPC 2000, Waters, Millford, USA, 418 K in 1,2,4-trichlorobenzene) universal to polystyrene and relative to polypropylene standards. The sample has a molecular weight of 100 kg/mol and M_w/M_n of about 2.1. NMR spectra were used to calculate the concentration of isotactic pentads. For this purpose 15 mg of the sample was dissolved in 500 μL toluene in a 5-mm tube. ^{13}C-NMR spectra were recorded on a Bruker AMX 500 spectrometer (Bruker GmbH, Rheinstetten, Germany) operating at 353 K. The analyzed sample contains 35% isotactic pentads.

Film preparation

Different types of films were used for the various analysis techniques. For WAXS investigations and for mechanical testing, melt-pressed films with a thickness of about 1 mm were used (Series A). The surface of these films was rough because of the

casting of the pressing tool. Therefore, these samples are not suitable for SFM experiments. For SFM experiments a second set of film was fabricated by combing solvent casting and heat-treating (Series B). All films were stored for 6 months at room temperature under ambient conditions (30% humidity, 278 K) prior to testing investigations to ensure that the samples were in thermal equilibrium (fully crystallized). For both types of films a crystallinity of about 18% has been determined from the first DSC run.

Melt-pressed films

To prepare melt-pressed films (Series A), 10 g of granulated polymer was placed in between two glass plates covered with PTFE foils and 1 mm spacer. The polymer was heated under constant low pressure (2 kN) to 390 K. Once the sample was molten, the pressure was increased up to 5 kN and held for 30 min. The pressure was increased up to 20 kN and held for another 30 min, after which the sample was cooled down to room temperature at a cooling rate of 1.5 K/min. The final thickness of the film was 1 ± 0.01 mm determined by a micrometer screw.

Solvent-casted films

Solvent-casted films were prepared by dissolving 2 g of the polymer in 75 mL of toluene. The solution was heated in a water bath to 350 K and held there for 60 min to ensure the total dissolution of the polymer. The solution was then casted on top of a PTFE foil, which was placed in a Petri dish (ø = 10 cm). The Petri dish was covered with glass to enable the slow evaporation of the solvent. After 7 days, films with a thickness of 0.25 ± 0.05 mm were obtained. To simulate the heating process of the melt-pressed film, the solvent-cast films were heated in a vacuum oven at 390 K for 60 min and cooled down to room temperature at a cooling rate of 1.5 K/min (Series B).

Mechanical characterization

To test the mechanical properties of the samples, stretching experiments were performed using commercial stretching device (Zwick 1445, Zwick GmbH + Co. KG, Ulm, Germany). Samples were punched using a dog-bone puncher from both films types (series A and B). The final specimens were 20-mm long and 5-mm wide. To calculate the nominal stress, the cross-sectional area has to be determined. Therefore, in addition to the width of the samples the exact thicknesses were estimated using a micrometer screw. The initial length of the sample and their elongation were measured by the optical detection system (accuracy of the method: ±0.5 mm) of the used stretching device. For this purpose, two optical markers were applied in the middle of the sample with a distance of around 15 mm. To determine the stress–strain behavior, the samples were subjected to tensile testing with a stretching rate of 4 mm/min until the sample failed.

To determine the reversible deformation and to study the morphology of stress-relaxed specimen, the samples were stretched to a desired strain rate ($\lambda_{cyc} = 8$) using a strain rate of 4 mm/min, hoöding the film under tension for 1 min, then unloading at a rate of 4 mm/min. Subsequently, the samples were removed from the testing machine and stored unloaded for 24 h to allow them to recover totally before measuring their final length (l_{rel}). The elasticity of a sample was defined as the amount of reversible strain ε_{rev} after elongation to a given strain rate λ_{cyc} calculated by eq. (1), where l_{cyc} is the length of the sample stretched to λ_{cyc} and l_{rel} is the length of the relaxed sample.

$$\varepsilon_{rev} = \left(\frac{l_{cyc} - l_{rel}}{l_{cyc}}\right) \times 100 \quad (1)$$

Equation for the calculation of the reversible deformation ε_{rev} after elongation to a given strain rate λ_{cyc}, to λ_{cyc} with l_{cyc} = length of the sample stretched and l_{rel} = length of the relaxed sample.

Wide angle X-ray scattering

For X-ray scattering experiments, 1-mm-thick melt-pressed films (series A) were used. Wide angle X-ray scattering (WAXS) measurements were performed at room temperature at the beamline A2 (wavelength = 1.5 Å, HASYLAB, DESY, Hamburg). Phosphor imaging-plate devices (IP) were used recording the two-dimensional (2D) scattering intensities. For stretching the melt-pressed films, a custom made setup was placed in the beamline. The sample was stretched stepwise from $\lambda = 1$ (non-stretched state) to $\lambda = 9.7$ ($\Delta\lambda \geq 1$). At each step, a 2D scattering record was taken. Sample elongation was determined using radiolucent markers on the strips and a caliper. The crystallinity of the sample in the nonstretched state, where the existing crystals exhibits an isotropic distribution, was determined according to the method described in Ref. 15. The crystallinity is given by the ratio of the integral of the scattering curve subtracted by the amorphous halo to the integral of the whole scattering curve.[15]

A constant azimuthally intensity distribution of the 2D scattering images assured that only initially isotropic samples were investigated. For a quantitative description of the orientation, radial intensity

distributions were collected and the orientation functions were calculated. Data acquisition and calculation of the orientation function were performed as described in detail in Ref. 55. Therefore, the azimuthal intensity distributions at the scattering angles of interest representing the main net planes (110_α, 040_α, and 202_γ) [sample P3 in Ref. 55] were determined from the radial intensity distributions. The orientation functions, which are the functions of the azimuthally intensity distribution, were calculated for each elongation step. The notations of the reflections given herein correspond to the identification of the apparent crystal modifications in the presented sample as analyzed from Boger et al.[15]

Orientation functions are presented as functions of elongation. The codomain of the orientation function ranges from −0.5 (net planes are perpendicular oriented to the reference axis) to 1 (net planes are parallel oriented to the reference axis). The reference axis was the stretching direction indicated by $\varphi = 0^\circ$. Zero ($f = 0$) indicates an isotropic distribution of the net planes. A rotational symmetry can be assumed if the sample dimensions are several times bigger than oriented structures according to.[60] This is the case for the presented polymer, where the sample thickness was greater than 0.1 mm even at maximum elongations.

Additionally, the superstructures of the samples were investigated under uniaxial deformation performing SAXS measurements. The SAXS records were made similar to the WAXS records with longer detector-sample distance and higher exposure time.

Scanning force microscopy

For scanning force microscopy (SFM) investigations, solvent crystallized films (series B) were used because their surfaces are relatively smooth and their surface morphology is the same as the volume structure detected in cryomicrotome cuts. Besides, the macroscopic properties determined from stress–strain experiments were similar to the ones observed for thicker melt-pressed films. To investigate the morphology of polypropylene samples, the surface of the solvent-casted films were imaged using a D3100 Scanning Probe Microscope equipped with a Nanoscope IIIa controller (Veeco Instruments, Santa Barbara, CA) under ambient conditions. The microscope was operated in tapping mode (TM) using standard microfabricated silicon cantilever with aluminum reflex coating (OMCL 160TS, Olympus Corporation, Japan). The cantilevers have nominal spring constants of 40 N/m; typical resonance frequencies ranged between 275 and 315 kHz. In TM[61] the topography is measured as the constant distance of the tip normal to the surface by keeping the amplitude of the oscillating tip constant. The amplitude damping r_{SP} conditions the applied force. The value r_{SP} is defined as the ratio of the engaged amplitude A to the free air amplitude (A_0) of the oscillating tip. The amplitude and the set point ratio were chosen such that the cantilever-tip assembly did not get trapped on the sample surface and that the imaging conditions warranted stiffness-dominated contrast in the phase images. In phase images recorded under these conditions, harder domains typically have higher phase shifts, thus appearing brighter than softer areas. For a discussion of image contrast and its dependence on scanning conditions see Refs. 62–68. In our studies the free amplitude A_0 has been set to 2 V, which is equivalent to 90 nm, and the set point amplitude A ranges between 1.325 and 1.35 V resulting in an amplitude damping r_{SP} of about 0.65–0.7. The phase images shown here were subjected to a first-order plane-fitting procedure to compensate for sample tilt. The magnitude of the phase signal is affected by various scan parameters, such as the precise amplitude of the free vibrating cantilever and the set point ratio. Since these values are given by the SFM software and cannot be absolutely controlled, the recorded values can only be considered as relative ones.[62–67] Thus, phase images are presented without an absolute color scale.

SFM images were performed on one sample (Series B) at different deformation states. Therefore a custom-built stretching device was combined with SFM to monitor deformation-induced changes in the morphology of polymeric films on-line.[69] The compact setup of the stretching device fits in a Dimension 3100 SPM (Veeco, Santa Barabra, USA).

Two computer controlled stepper motors (MICOS GmbH, Eschenbach, Germany) were used for stretching. This balanced assembly was used to secure symmetric deformation of the sample. A strain gauge force sensor with a maximum range of 5 ± 0.5 N (Submidget force sensor Type 8411, Burster, Gernsbach, Germany) equipped with an integrated amplifier (SEMMEG 9000). The stretching device was controlled via custom-built software, which allows the simultaneous recording of force and strain. This enables it to measure either the force-elongation curves of the used samples or to control the force during SFM imaging. The latter has been shown to be an important parameter because previous deformation experiments of elastic materials show that these samples relax when the stretching process was interrupted. To avoid relaxation-induced changes in sample structure while scanning, the specimen was left under a given strain for at least 3 h to relax. To retain relatively high surface smoothness and avoid film vibrations, a moveable support has been mounted in the middle of the stretching device where the height can be adjusted by a micrometer screw.

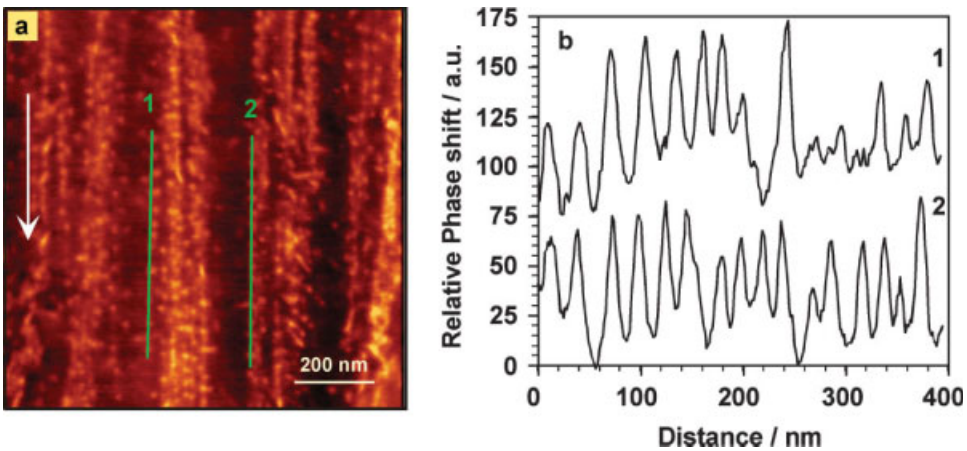

Figure 1 The phase shift images (a), where the crystalline blocks appear as bright spots were used to analyze the local deformation. Therefore, the average distance of crystalline blocks was determined from cross-sectional plots (line 1 and 2 in (a,b)) along the stretching direction, which is indicated by an arrow. [Color figure can be viewed in the online issue, which is available at www.interscience.wiley.com.]

The morphological changes were recorded by taking a series of phase shift images of the film surface after stepwise stretching from $\lambda = 1$ to $\lambda = 7$. The elongation was determined by the initial length (l_0) and the displacement (Δl) received from the calibrated step motor control (accuracy: ± 1 mm). Stress-relaxed specimens have been prepared by stretching the film up to $\lambda = 8$, keeping them under tension for 1 min at room temperature, unloading, and allowing the specimens to relax for 2 h.

The average distance between adjacent crystalline blocks was detected by means of line scans of SFM phase images [Fig. 1(a,b)]. The results are averaged over at least 10 crystalline domains. SFM phase images of the samples were performed on a scan range of 1 μm with 512 × 512 pixels per image. Any quantitative determination of the lamellar dimensions from TM-SFM images leads to a considerable overestimation because of the finite tip radius.

RESULTS AND DISCUSSION

Mechanical testing

Similar stress–strain curves were obtained for melt-pressed and solvent-crystallized films when they were stretched until they failed [Fig. 2(a)]. The stress–strain curves show clearly that the samples can be assigned to the group of elastomers, because the obtained stress–strain curve does not show a pronounced yield point, but after reaching an elastic plateau the stress increases continuously until the sample fails after stretching up to 10 times of its initial length. Comparing melt-pressed films and the

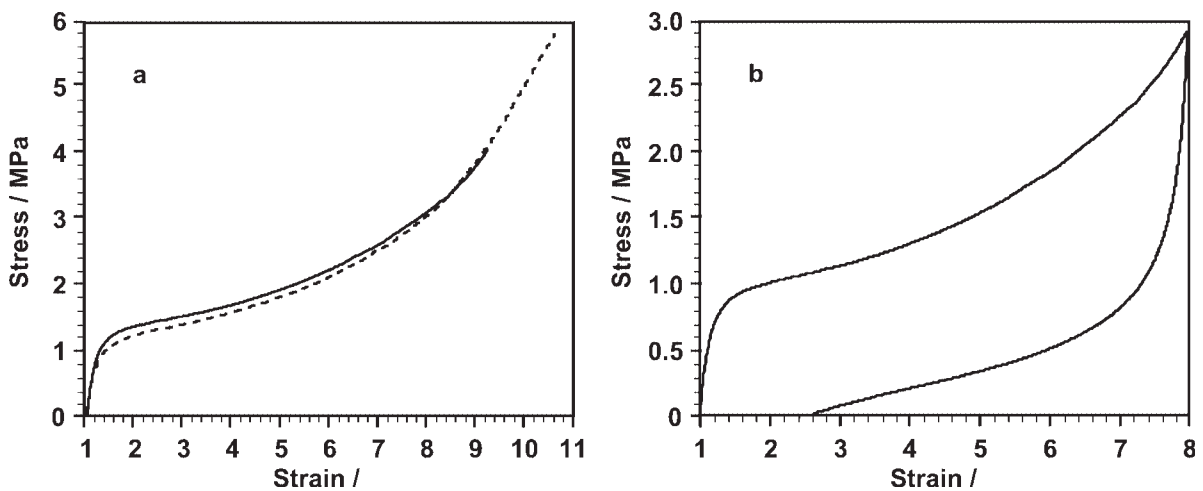

Figure 2 Stress–strain curves of tensile test until failure (a) received from a melt-pressed sample (Series A, dotted line) and from a solvent-casted sample (Series A, full line) show similar stress–strain behavior. Cyclic tensile test from a solvent-casted sample (b) reveals a high elastic recovery.

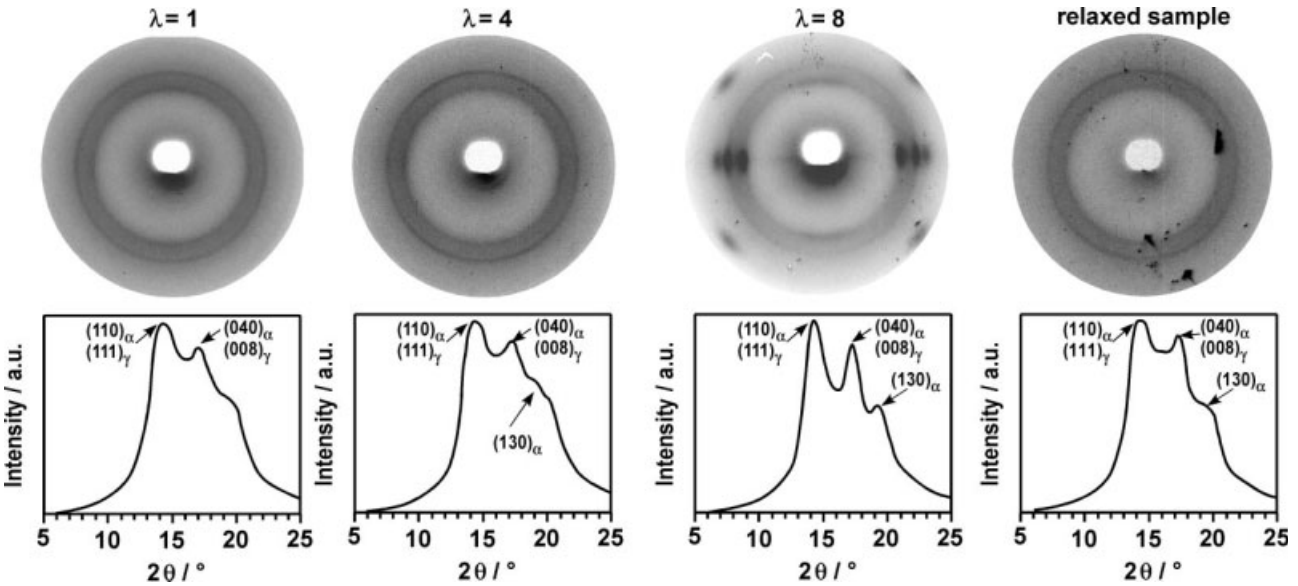

Figure 3 Two days WAXS-images of the sample at elongations of $\lambda = 1$, 4, and 8 and in the relaxed state (top). Equatorial radial intensity distributions at elongations of $\lambda = 1$, 4, and 8, and in the relaxed state (bottom).

ones obtained from solution crystallization, both types reached maximum strains up to $\lambda = 10$ to 12 before the specimen fails at failure stresses σ_{max} of about 6 ± 1 MPa. Mentioned similarities showed that the internal structure, which mainly determines the mechanical behavior of a polymer, could be assumed to be the same for the different processing techniques. This presents a major requirement for the presented study, because X-ray scattering techniques collect information from the bulk material and SFM near the surface of the sample. Thus, the solvent-crystallized films can be used as a model system for SFM experiments.

The reversible deformation [Fig. 2(b)] was determined as described in the experimental section. A reversible deformation of $75\% \pm 5\%$ was observed for all the investigated samples indicating a high reversible deformation.

WAXS

Sample material investigated herein presented a crystallinity of around 18%, which agreed well to the amount of hard segments derived from the SFM investigations. Figure 3 (top) shows 2D WAXS-images of the sample at various states of elongations from $\lambda = 1$ to 8 and after unloading. The WAXS measurements showed very distinctive fiber textures for the sample presented. Orientation of the crystals could be obtained qualitatively by the scattering patterns which become anisotropic, or in other words the azimuthal intensity distribution is not constant anymore. Additionally, the equatorial radial intensity distributions at the several stretching steps are shown (Fig. 3, bottom). The sample indicates reorientation and recrystallization at elongation lower than $\lambda = 4$, which could be seen qualitatively due to the alteration of the radial intensity distributions.

Quantitative orientations of the net planes are presented using the orientation function as a function of the elongation (Fig. 4). Orientation functions calculated for the sample of the main net planes $(110)_\alpha$, $(040)_\alpha$, and $(202)_\gamma$ are shown in Figure 4. An actual value of the orientation function nearly zero in the unstretched sample ($\lambda = 1$) shows an initially isotropic state of the sample. When the sample is stretched to $\lambda = 2.5$, the change from zero indicates that the scattering becomes anisotropic due to orientation of the existing crystals. During stretching, the $(110)_\alpha$ net planes orient themselves toward the stretching direction ($f < 0$) and become more accurate at higher elongations. Net planes corresponding

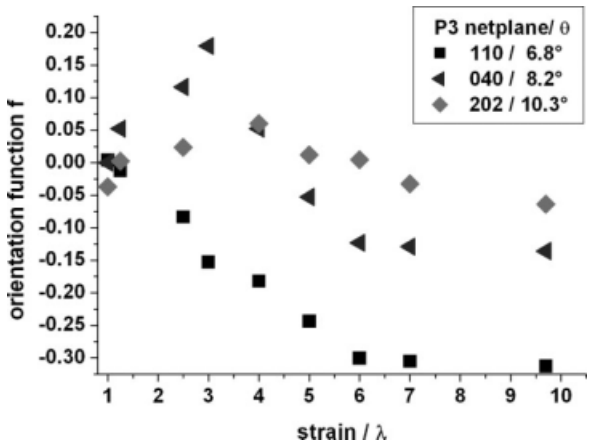

Figure 4 Orientation functions on elongation from the $(110)_\alpha$, $(040)_\alpha$, and $(202)_\gamma$ net planes of the sample presented as received from a previous study.[55]

to $(202)_\gamma$ show a slight orientation ($f_{(202)\gamma} = -0.06$, $\lambda = 9.7$) even at maximum elongation. The orientation function of the net planes $(110)_\alpha$ decreases continuously to -0.31 at maximum elongation indicating a medium orientation along the stretching direction. The orientation observed from the net planes defined by $(040)_\alpha$ is the most interesting one. Those initially shows a slight orientation perpendicular to the stretching direction ($f = 0.18$, $\lambda = 3$) and a decrease afterwards ($f = -0.14$, $\lambda = 9.7$). The orientation of the $(040)_\alpha$ net planes that should occur exclusively on the equator are not completely understood. These reflexes can be caused by tilted crystal structures such as lath-like crystals formed due to the failure of the crystalline lamella. The authors would also like to mention that these reflexes can be overlapped with others at this scattering angle region (e.g. $(110)_\alpha$, which can be present in several orientation directions in the a_α-axis + c_α-axis orientation[70]). Separation of the WAXS reflexes belonging to different origins is very difficult, e.g., different sized lamella occurring during stretching as mentioned in the SFM results cannot be separated by presented WAXS investigations. Uniform chain orientation for $\lambda > 4$ where all blocks and tie chains are aligned toward the stretching direction, as an optimization of the fibrillar structure are consistent with SFM observations.

The stress–strain curve of the sample (Fig. 2) shows a steadily increase in strength after reaching $\lambda = 3$. Comparing the slope of the stress–strain curve and the orientation of the $(110)_\alpha$ net planes it can be concluded that the increase in crosslinking density (increasing slope/material stiffness) is associated with constant increasing orientation of the $(110)_\alpha$ net planes, which consists mainly of α-crystals.[15] This indicates that the arrangements of the amorphous and crystalline phases which are connected to this particular crystal orientation mainly cause the driving force, which could be the reason for the elasticity after stress is released. Those oriented crystals could be only a part of all crystals, especially only the small crystals, which are formed during stretching as mentioned in the SFM results and discussion section. But it is thought that they mainly contribute to the blocks, building the network which is responsible for material elasticity. According to the findings described in Ref. 55, the sample showed a parallel chain axis-orientation of the disordered α/γ-crystals according to the calculations from Auriemma and De Rosa.[70] Changes of the orientation function belonging to net planes called $(040)_\alpha$ showed also a high correlation to the stiffness of the material and have to be analyzed and understood in more detail.

A WAXS record performed in the relaxed state after stretching to $\lambda = 8$ is shown in Figure 3. Presenting extended sickle-shaped reflexes produced by same net-planes instead of several dots show, that if the stress is released, the crystals are stable but relaxed in the orientation. Orientation functions calculated for the main net planes (not shown) in the relaxed state decreased to $f = -0.1$ and $f = -0.08$ for the net planes defined by $(110)_\alpha$ and $(040)_\alpha$, respectively. Orientation function for the $(202)_\gamma$ net planes remained constant after releasing the stress ($f = -0.05$). Keeping the sample under tension at high elongation over longer time, further crystallization appears which can qualitatively be observed as an increase of the peak height and therefore of the reciprocal integral width which is directly related to the crystal size.[15]

SAXS records showed no discrete scattering reflexes and therefore no indication on existing superstructures could be observed by the X-ray scattering investigations.

Scanning force microscopy

The sequence of SFM images of solvent-crystallized sample under deformation and in the relaxed state is shown in Figure 5(a–i).

The phase shift image of the unstretched sample [Fig. 5(a), $\lambda = 1$] shows isotropic dispersed but discontinuous hard domains consisting of rod-like crystalline lamellae and smaller crystalline blocks immersed in a continuous softer, most likely amorphous phase. The determined amount of hard phase was about 18% ± 2% of the surface. These data suggest that owing to the relatively low isotacticity the crystalline lamellae and blocks form a network-like structure.[41] Stretching to $\lambda = 1.5$ results in the re-orientation of some of the crystalline lamellae parallel to the stretching direction, but most of them remain unoriented [Fig. 5(b)]. Similar trends can be observed at $\lambda = 2$, but here the orientation of the larger crystalline domains [Fig. 5(c)] becomes more obvious. Tilting of the lamellae occurs in such a way that the chain folds are aligned with the tensile axis. This parallel alignment of the chain is supported by the X-ray experiments.

Within this deformation regime the stress increases nearly linearly with the strain up to a maximum level of 1.2 MPa [Fig. 2(b)]. This suggests that at this state of deformation mainly tie chains within the amorphous regions become extended. When a distinct level of stress was reached, additionally the separation between crystalline segments occurs as shown in Figure 5(d) and the stress stays nearly constant (Fig. 2). The SFM image recorded at $\lambda = 3$ shows that only a few large lamellae remain unchanged, preferably those aligned parallel to the stretching direction. Almost no crystal retains its

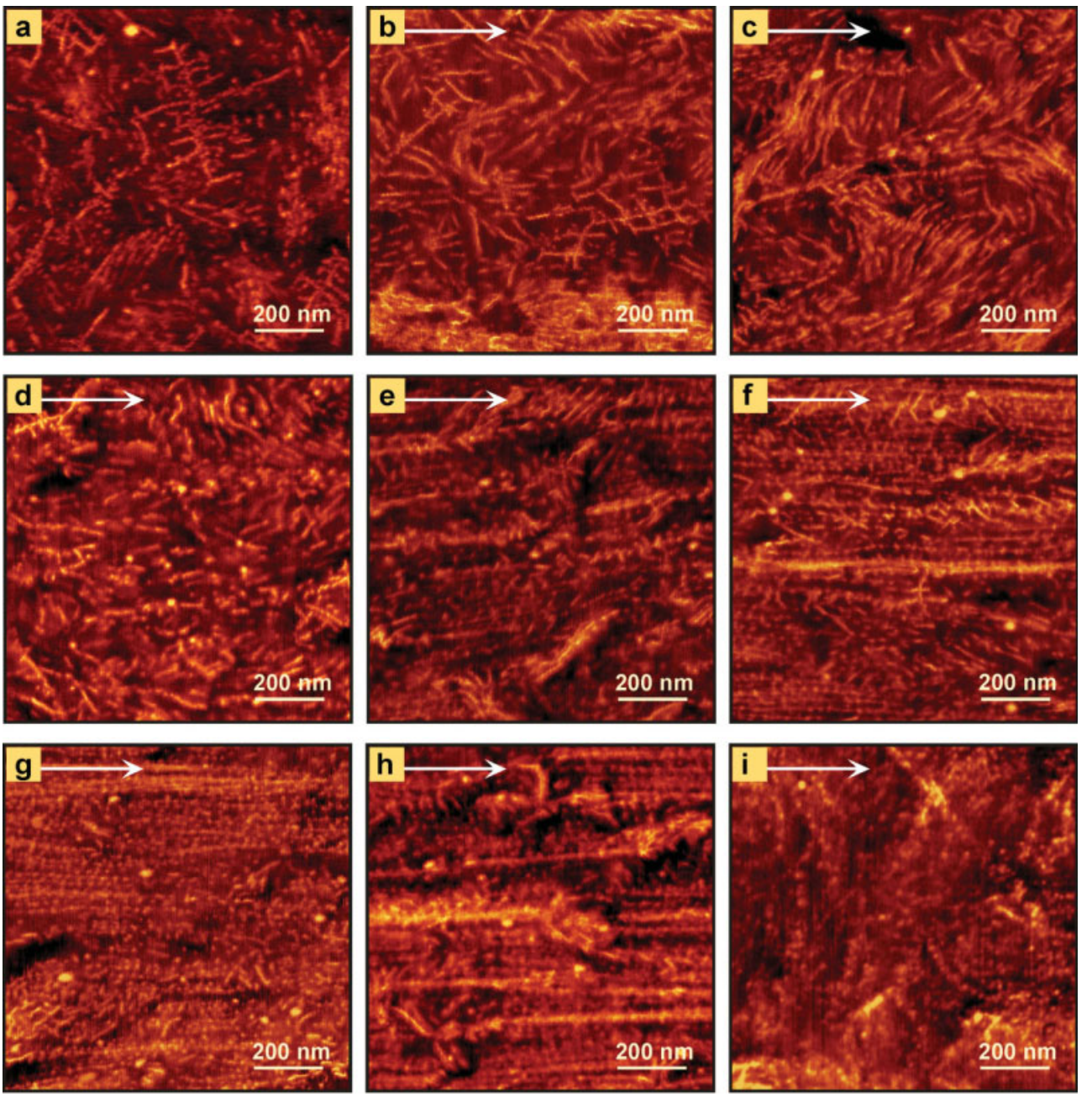

Figure 5 SFM phase images reveal the morphological changes at increasing elongation $\lambda = 1$ (a) to $\lambda = 7$ (h) and in the relaxed state (i). Arrow indicates the stretching direction. [Color figure can be viewed in the online issue, which is available at www.interscience.wiley.com.]

original length. Therefore, at this strain the stress was sufficient to break up the initial ribbon-like crystals into small blocks. The constant increase in stress observed in the stress–strain curve (Fig. 2) points out that the local stress required to break a given crystallite becomes higher when the crystallite size decreases. When the sample is stretched to $\lambda = 4$, almost all of the original crystallites are destroyed [Fig. 5(e)]. However, they are not all transformed in small blocks with an average width of 7 ± 2 nm until a draw ratio $\lambda = 5$ is reached [Fig. 5(f)].

The images taken at a draw ratio $\lambda = 6$ [Fig. 5(g)] show blocks connected by strings resembling in fibrillar structures which are aligned in the stretching direction. The fibrils are reminiscent on a beads-on-a string structure where the crystalline blocks are detected as the slightly wider regions (beads) connected by slightly darker strings. The strings have a width in the narrow direction about half of the block width. These thinner microfibrils oriented in the strain direction might consist of originally amorphous sequences.[42,71] Since SFM phase shift images

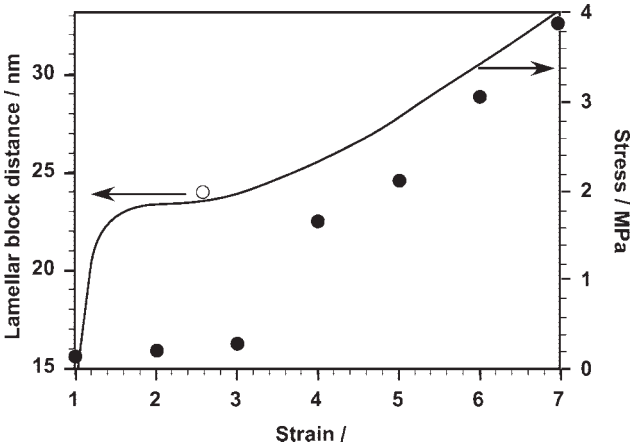

Figure 6 Averaged distance between adjacent crystalline/lamellar blocks along the stretching direction as function of the strain (filled circles) and in the relaxed state (open circle). Stress–strain diagrams of tensile test until failure (line).

are sensitive only to changes in local stiffness, lamellar crystals as well as oriented soft segments could both appear to be "stiff" enough to provide contrast. In the final stage of elongation ($\lambda = 7$) almost all blocks and tie chains are aligned along the direction of the tensile axis resulting in a highly oriented fibrillar structure depicted in Figure 5(h). Since the fibrils are perfectly straight, they have to be under stress. This structure is very similar to the load-bearing microfibrils imaged by electron microscopy in highly oriented ultrathin polyethylene.[48,49] Thus, the morphology formed at high strains is similar to the fibrillar structure observed for higher crystalline samples.

The closer examination of the microfibrillar structure points out that at increasing elongation the distance between adjacent crystalline blocks increases along the stretching direction. This suggests the continuous elongation of the amorphous domains at increasing draw ratios. To quantify the local deformation in the stretching direction, the distance between crystalline blocks along the stretching direction was determined from cross-sectional plots (Fig. 1). Plotting the distances versus the elongation, strain-induced microscopic changes in morphology (filled circles, Fig. 6) can be correlated to the macroscopic stress–strain behavior (line, Fig. 6).

Within the deformation regime between $\lambda = 1$ and 3, the distance between adjacent crystalline blocks along the stretching direction is nearly unchanged. Since the amorphous regions become elongated and rod-like lamellae are oriented parallel to the stretching direction [Fig. 5(a–c)] it can be suggested that within this stretching regime the local stress is insufficient to break up the crystalline lamellae. A substantial increase in the distance between adjacent crystalline blocks can be observed when the strain increases from $\lambda = 3$ to 4. Thus, the local stress becomes high enough to break the lamellae apart and lamellar blocks are formed which start to align along the stretching direction. The fractions are displaced and their distance increases when the strain becomes larger. The additionally observed increase in stress can be attributed to the fact that the smaller, thus shorter the lamellae, the higher the stress necessary to break them up.

When the strain $\lambda > 4$, microblocks are formed all over the sample which are aligned along the stretching direction revealing a fibrillar superstructure [Fig. 5(f–h)]. The increase in strain leads to a nearly linear increase in stress and in block distance along the stretching direction. Since no further crystalline break up can be observed in the SFM images, it might be suggested that the amorphous chains connecting the microblocks are elongated in the same ratio as the macroscopic draw ratio increase until at the deformation of $\lambda = 7$. At this strain, the flexible chain segments are aligned nearly perfectly parallel and form a microfibrillar structure [Fig. 5(h)]. The aligned chains start to crystallize due to the applied stress, and the increase in block distance is no longer linear (not shown here).

To learn more about the elastic recovery of the films, a stress-relaxed specimen has been prepared. An elastic recovery ε_{rev} of 75% ± 5% of the sample refers to irreversible changes in the polymer structure during deformation. SFM phase shift images of a relaxed sample [Fig. 5(i)] confirm the results, which were just mentioned already. In the image taken in the relaxed state, the degree of reversibility of the structure orientation is visualized. After releasing the stress, the extended amorphous domains contract and the most part of the sample reveals randomly distributed crystalline blocks [Fig. 7(a)]. Thus, the entropy-driven relaxation of the amorphous interspaces can be proposed. Within some areas oriented fibrils with a beads-on-a-string structure persist [Fig. 7(b)]. Along the fibrils the average distance between the individual crystalline blocks is reduced compared to the stretched state (open circle, Fig. 6). The distance is larger than the one estimated in the unstretched state: It might be suggested that some fraction of the amorphous chains crystallized under stress and cannot entropically relax. Thus, for the relaxation morphological changes due to melting and recrystallization might be taken into account. Examination of the increase in crystallinity due to stress crystallization as it was suggested for this material[55] has to be analyzed in further studies which will lead to a better base for the current interpretations.

The results of WAXS and SFM support the proposed model for the deformation of thermoplastic

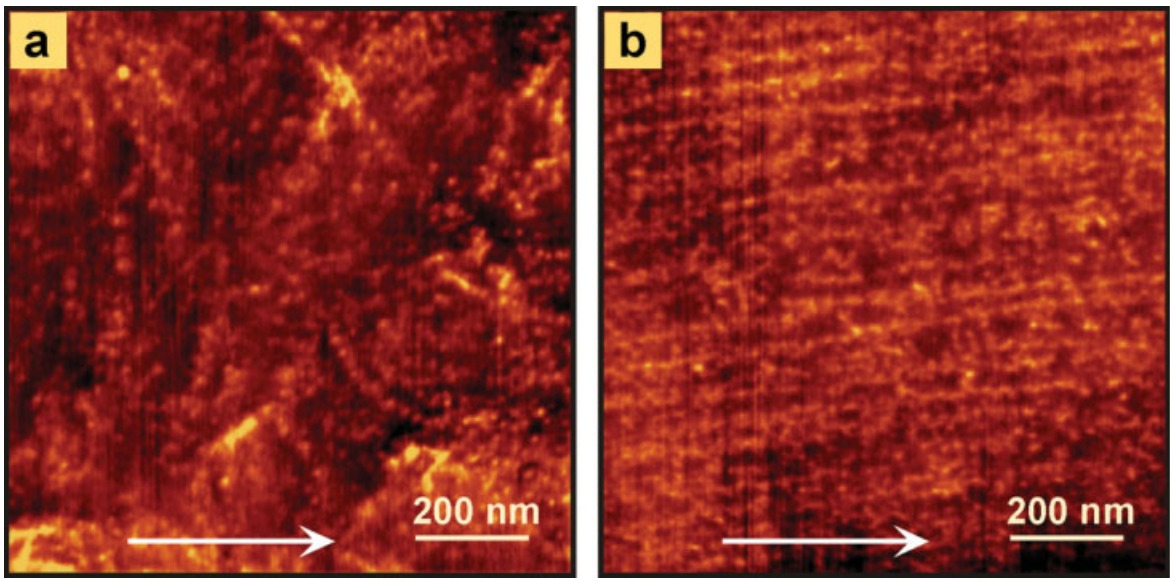

Figure 7 SFM phase images to illustrate that after relaxation domains consisting of either randomly distributed crystalline blocks (a) or of still aligned fibrils (b) can be found. Later might be due to stress induced crystallization. Arrow indicates the stretching direction. [Color figure can be viewed in the online issue, which is available at www.interscience.wiley.com.]

elastic polymers[28,53–55] but in the case of the homogeneous crystalline network some modifications are necessary (Fig. 8). Under low deformation, the amorphous regions are extended and crystalline lamellae rotate to become aligned with their long axis parallel to the stretching direction. Thus, the chains are oriented perpendicular to the stretching direction [Fig. 8(b)] At higher elongation [Fig. 8(c)] the lamellae are preferably oriented perpendicular to the stretching direction. Because of the local stress the crystalline domains break up and small blocks are formed. At further elongation [Fig. 8(d)] a fibrillar

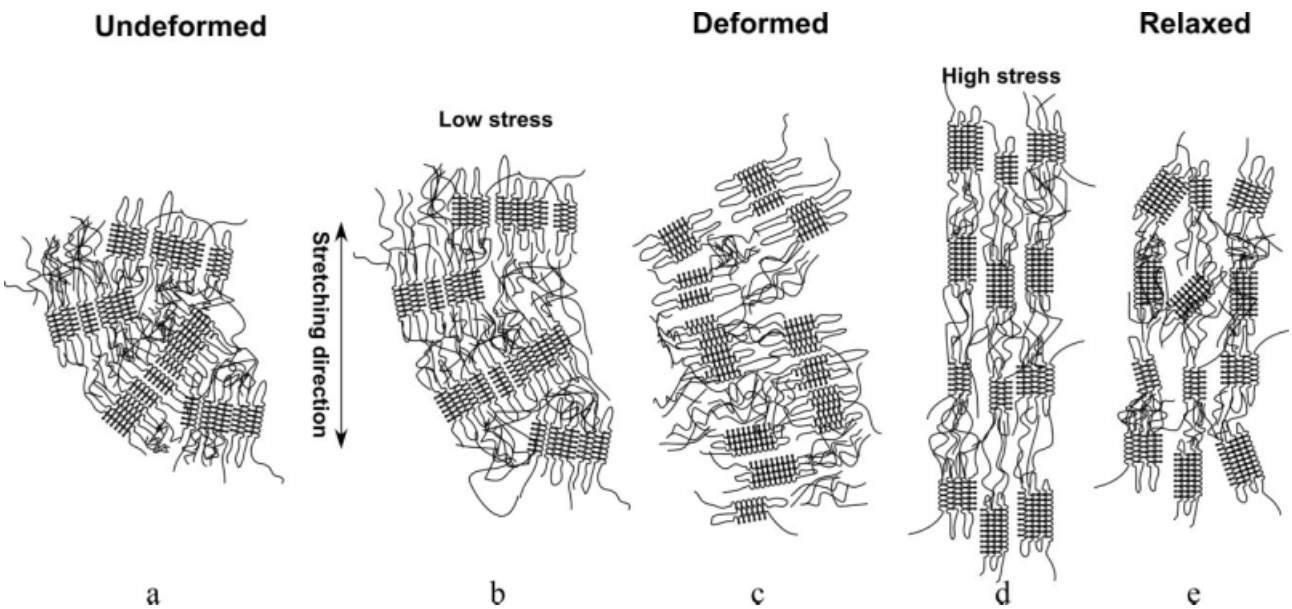

Figure 8 Schematic of the deformation-induced changes in morphology of low isotactic polypropylenes: (a) Undeformed film. (b) Under low deformation the amorphous regions are extended and long axis of the crystalline lamellae start to orient parallel to the stretching (c). At higher elongation small blocks aligned in fibrillar superstructure are formed where chains orient parallel with the stress direction (d). Releasing the stress, preferably the amorphous domains are retracted (e).

superstructure is formed where chains oriented parallel to the strain direction and the soft segment chains will undergo stress-induced crystallization. Releasing the stress [Fig. 8(e)], the amorphous domains are preferably retracted.

Orientation of the existing structures could be shown with both methods and also correlated to the macroscopically properties. However a strengthening effect on the interpretations by combining those methods could only partly observed.

CONCLUSIONS

These results obtained from WAXS studies in combination with the SFM experiments lead to the conclusion that the proposed structural model for the deformation of low-crystalline polymers also fits for low iPP with randomly distributed stereoerrors. Since the isotactic blocks are short, only small lamellar domains can be formed. These lamellar blocks are the reason for a randomly distributed continuous network, which showed much higher elasticity and failure strain compared to the stereoblock polypropylenes investigated up to now.[6] The improved elastic properties compared to stereoblock polypropylenes are mainly caused by the homogeneously distributed crytalline crosslinks.

The SFM experiments give strong evidence that randomly distributed microblocks are not only initially formed during crystallization from solution or melt, but generated by crystallite breakup and orientation of small crystalline blocks when the samples are stretched for the first time. In following stretching experiments these microblocks act as crosslinks and chain segments belonging to the amorphous phase, connecting the crystalline regions are elastically deformed. They act as springs between the crystals, which are in extended conformation in the stretched state and return in the disordered coil conformation when the tension is removed. Thus, the investigated low isotactic sample with a *mmmm* content of 35% confirms the model that the elastic recovery of TPEs occurs mainly due to the entropy-driven relaxation of the amorphous segments.

Since the breakup of crystallites is essentially irreversible, plastic deformation contributes to the reduction elastic recovery (ε_{rev}) between the first and second deformation cycle.[55]

References

1. Lin, C. Y.; Chen, M. C.; Mehta, A. K. J Plast Film Sheet 2001, 17, 113.
2. De Rosa, C.; de Ballesteros, O. R.; Auriemma, F.; Savarese, R. Macromolecules 2005, 38, 4791.
3. De Rosa, C.; Auriemma, F.; Perretta, C. Macromolecules 2004, 37, 6843.
4. Auriemma, F.; de Ballesteros, O. R.; De Rosa, C. Macromolecules 2001, 34, 4485.
5. Müller, G.; Rieger, B. Prog Polym Sci 2002, 27, 815.
6. De Rosa, C.; Auriemma, F.; Spera, C.; Talarico, G.; Tarallo, O. Macromolecules 2004, 37, 1441.
7. Brintzinger, H. H.; Fischer, D.; Mülhaupt, R.; Rieger, B.; Waymouth, R. M. Angew Chem Int Ed Engl 1995, 34, 1143.
8. Dietrich, U.; Hackmann, M.; Rieger, B.; Klinga, M.; Leskelä, M. J Am Chem Soc 1999, 21, 4348.
9. Rieger, B.; Troll, C.; Preuschen, J. Macromolecules 2002, 35, 5742.
10. Dietrich, U. Synthesis of Novel C2 and Unsymmetric ansa-Zirconocenes—Application in Homogeneous Catalysis for the Production of Isotactic and Thermoplastic Elastic Polypropylene, Shaker Verlag GmbH: Germany, 1999. ISBN 3–8265-4928–7.
11. Mallin, D. T.; Rausch, M. D.; Lin, Y. G.; Dong, S. H.; Chien, J. C. W. J Am Chem Soc 1990, 112, 2030.
12. Coates, G. W.; Waymouth, R. M. Science 1995, 267, 217.
13. Schnutenhaus, H.; Brintzinger, H. H. Angew Chem 1997, 91, 837.
14. Wild, F. R. W. P.; Zsolnai, L.; Huttner, G.; Brintzinger, H. H. J Organomet Chem 1982, 232, 233.
15. Krukral, J.; Rieger, B. Macromol Symp 2002, 177, 71.
16. Boger, A.; Heise, B.; Troll, C.; Marti, O.; Rieger, B. Eur Polym J 2007. 43, 634.
17. Ewen, J. A.; Elder, M. J.; Jones, R. L.; Haspeslagh, L.; Atwood, J. L.; Bott, S. J.; Robinson, K. Makromol Chem Macromol Symp 1991, 48/49, 253.
18. Kaminsky, W. Macromol Chem Phys 1996, 197, 3907.
19. Resconi, L.; Cavallo, L.; Fait, A.; Piemontesi, F. Chem Rev 2000, 100, 1253.
20. Natta, G.; Mazzanti, G.; Crespi, G.; Moraglio, G. Chim Ind (Milan) 1957, 39, 275.
21. Natta, G. U.S. Pat. 3,175,999 (1965).
22. Natta, G. J Polym Sci 1959, 34, 531.
23. Collette, J. W.; Tullock, C. W. (Dupont) U.S. Pat. 4,335,225, (1982).
24. Tullock, C. W.; Mülhaupt, R.; Ittel, S. D. Makromol Chem Rapid Commun 1989, 10, 19.
25. Tullock, C. W.; Tebbe, F. N.; Mülhaupt, R.; Ovenall, D. W.; Setterquist, R. A.; Ittel, S. D. J Polym Sci Part A: Polym Chem 1989, 27, 3063.
26. Collette, J. W.; Tullock, C. W.; MacDonald, R. N.; Buck, W. H.; Su, A. C. L.; Harrel, J. R.; Mülhaupt, R.; Anderson, B. C. Macromolecules 1989, 22, 3851.
27. Collette, J. W.; Ovenall, D. W.; Buck, W. H.; Ferguson, R. C. Macromolecules 1989, 22, 3858.
28. Llinas, G. H.; Dong, S. H.; Mallin, D. T.; Rausch, M. D.; Lin, Y. G.; Winter, H. H.; Chien, J. C. W. Macromolecules 1992, 25, 1242.
29. Kravchenko, R. L.; Sauer, B. B.; McLean, R. S.; Keating, M. Y.; Cotts, P. M.; Kim, Y. H. Macromolecules 2000, 33, 11.
30. Schönherr, H.; Wiyatno, W.; Pople, J.; Frank, C. W.; Fuller, G. G.; Waymouth, R. M. Macromolecles 2002, 35, 2654.
31. Schönherr, H.; Waymouth, C. J.; Frank, C. W. Macromolecules 2003, 36, 2412.
32. Baeurle, S. A.; Hotta, A.; Gusev, A. A. Polymer 2005, 46, 4344.
33. Bravakis, A.; Bailey, L. E.; Pigeon, M.; Collins, S. Macromolecles 1998, 31, 1000.
34. Gauthier, W. J.; Collins, S. Macromol Symp 1995, 98, 223.
35. Gauthier, W. J.; Collins, S. Macromolecules 1995, 28, 3779.
36. Gauthier, W. J.; Corrigan, J. F.; Taylor, N. J.; Collins, S. Macromolecules 1995, 28, 3771.
37. Chien, J. C. W.; Llinas, G. H.; Rausch, M. D.; Lin, Y. G.; Winter, H. H.; Atwood, J. L.; Bott, S. G. J Polym Sci Part A: Polym Phys 1992, 30, 2601.
38. Chien, J. C. W.; Llinas, G. H.; Rausch, M. D.; Lin, G. Y.; Winter, H. H. J Am Chem Soc 1991, 113, 8569.
39. Babu, G. N.; Newmark, R. A.; Cheng, H. N.; Llinas, G. H.; Chien, J. C. W. Macromolecules 1992, 25, 7400.

40. Balboni, D.; Moscardi, G.; Baruzzi, G.; Braga, V.; Camurati, I.; Piemontesi, F.; Resconi, L.; Nifant'ev, I. E.; Venditto, V.; Antinucci, S. Macromol Chem Phys 2001, 202, 2010.
41. Resconi, L.; Moscardi, G.; Sylvestri, R.; Balboni, D.Patent Montell 2000, International Patent Application.
42. Hild, S.; Cobzaru, C.; Troll, C.; Rieger, B. In Catalysis for Stereoregulating Polymerization; Baugh, L. S., Canich, J. M., Coughlin, E. B., Eds.; CRC Press, Taylor Francis Group: Boca Raton, FL, 2006; Chapter 9, p 231.
43. Men, Y.; Rieger, J.; Strobl, G. Phys Rev Lett 2003, 91, 95502.
44. Cayrol, B.; Petermann, J. J. J Polym Sci Polym Phys Ed 1974, 12, 2169.
45. Gohil, R. M.; Petermann, J. J. J Polym Sci Polym Phys Ed 1979, 17, 525.
46. Zhou, H.; Wilkes, G. L. J Mater Sci 1998, 33, 287.
47. Adams, W. W.; Yang, D.; Thomas, E. D. J Mater Sci 1986, 21, 2239.
48. Brady, J. M.; Thomas, E. L. J Mater Sci 1989, 24, 3311.
49. Peterlin, A. J Polym Sci 1969, 7, 1151.
50. Peterlin, A. J Mater Sci 1971, 6, 490.
51. Petermann, J.; Gohil, R. M.; Massud, M.; Goeritz, D. J Mater Sci 1982, 17, 100.
52. Miles, M. J.; Petermann, J.; Gleiter, H. J. J Macromol Sci Phys 1976, 12, 549.
53. Geddes, A. J.; Parker, K. D.; Atkins, E. D. T.; Beighton, E. J Mol Biol 1968, 32, 343.
54. McLean, R. S.; Sauer, B. B. J Polym Sci Part B: Polym Phys 1999, 37, 859.
55. Cella, R. J. J Polym Sci Part C: Polym Symp 1973, 42, 727.
56. Boger, A.; Heise, B.; Troll, C.; Marti, O.; Rieger, B. Eur Polym J 2007, 43, 3573.
57. Jandt, K. D.; Buhk, M.; Miles, M. J.; Petermann, J. Polymer 1994, 35, 2458.
58. McLean, R. S.; Sauer, B. B. Macromolecules 1997, 30, 8314.
59. Hild, S.; Gutmannsbauer, W.; Lüthi, R.; Furhmann, J.; Güntherodt, H. J. J Polym Sci Phys Ed 1996, 34, 1953.
60. Hild, S.; Rosa, A.; Marti, O. In Scanning Probe Microscopy of Polymer; Ratner, B. D., Tsukruk, V. V., Eds.; Oxford University Press: New York, 1998; Vol. 694, p 110.
61. Heise, B.PhD Dissertation, University of Ulm, 1972.
62. Zhong, Q.; Inniss, D.; Kjoller, K.; Elings, V. Surf Sci 1993, 290, L688.
63. Morkved, T. J.; Jaeger, H. M. Europhys Lett 1997, 40, 643.
64. Cleveland, J. P.; Anczykowski, B.; Schmid, A. E.; Elings, V. B. Appl Phys Lett 1998, 72, 2613.
65. Tamayo, J.; Garcia, R. Appl Phys Lett 1997, 71, 2394.
66. Tamayo, J.; Garcia, R. Appl Phys Lett 1998, 73, 2926.
67. Garcia, R.; Tamayo, J.; San Paulo, A. Surf Interface Anal 1999, 27, 312.
68. Scott, W. W.; Bhushan, B. Ultramicroscopy 2003, 97, 151.
69. Bar, G.; Thomann, Y.; Brandsch, R.; Cantow, H. J.; Whangbo, M. H. Langmuir 1997, 13, 3807.
70. Imhof, C. S. PhD Thesis, University of Ulm, 2005.
71. De Rosa, C.; Auriemma, F. Macromolecules 2006, 39, 7635.
72. Michler, G. H.; Godehardt, R. Cryst Res Technol 2000, 35, 863.